Three-dimensional finite element simulation of magnetotelluric fields incorporating digital elevation models

S. Kütter, A. Franke-Börner, R.-U. Börner, K. Spitzer

Institut für Geophysik, TU Bergakademie Freiberg, Gustav-Zeuner-Str. 12, 09599 Freiberg

1 Introduction

Pronounced topography may have an important impact on the magnetotelluric (MT) response and its neglect may lead to severe misinterpretations. Common simulation techniques based on rectangular grids are generally not well suited to deal with arbitrary geometry. We therefore use vector finite element (FE) schemes formulated on unstructured grids to cope with realistic topography and/or bathymetry. As an example, we have chosen the volcanic island of Stromboli which is located in the Mediterranean Sea off the west coast of Italy. Stromboli is an extreme electric environment with very conductive sea water surrounding the steep topography of the resistive volcanic edifice. Moreover, the varying bathymetry and the topography of the other islands of the Liparian archipelago cause distinct effects on the magnetotelluric response. Due to the large conductivity contrast and these extraordinary features it can be expected that the magnetotelluric apparent resistivities as well as the phases show a very complex behaviour. The objective of this work is to incorporate digital elevation models of this area into our numerical MT simulations allowing for a realistic look at the electromagnetic (EM) induction phenomena in such a complicated environment. On top of its challenge for numerical simulation methods this volcano has always fascinated geoscientists (Fig. 1) and future interdisciplinary studies aim at investigating the inner structure and the processes that lead to the continuous mild eruptions recorded over the last 2 000 years (the so called 'Strombolian activity').

Figure 1: Map of the Aeolian Islands (left, Wikipedia (2010)) and Stromboli (right, SwissEduc (2010))

2 Physical and numerical basics

Based on Maxwell's equations and assuming a harmonic time dependency $e^{i\omega t}$ of the incoming plane wave, the equation of induction in terms of the vector potential $\mathbf{A}$ reads as

$$\nabla \times \mu^{-1}(\nabla \times \mathbf{A}) + (i\omega\sigma - \omega^2\varepsilon)\mathbf{A} = 0, \tag{1}$$

where $\mu, \sigma, \varepsilon, \omega$ and i are the magnetic permeability, the electric conductivity, the permittivity, the angular frequency and the imaginary unit, respectively. The magnetic field $\mathbf{H}$ and the electric field $\mathbf{E}$ are obtained by

$$\mathbf{H} = \mu^{-1}(\nabla \times \mathbf{A}) \quad \text{and} \quad \mathbf{E} = -i\omega\mathbf{A} - \nabla V. \tag{2}$$

The scalar potential V was eliminated from eq. (1) by the gauge condition $\psi = -iV/\omega$ and substituting $\mathbf{A}$ for $\mathbf{A} - \nabla\psi$ which leaves $\mathbf{H}$ and $\mathbf{E}$ unchanged.

23. Schmucker-Weidelt-Kolloquium für Elektromagnetische Tiefenforschung,
Heimvolkshochschule am Seddiner See, 28 September - 2 Oktober 2009

60

To calculate $\mathbf{A}$ in a bounded domain $\Omega \subset \mathbb{R}^3$, electric and magnetic insulation are required for all outer boundaries parallel ($\Gamma_{||}$) and perpendicular ($\Gamma_{\perp}$) to the current flow, respectively:

$$\mathbf{n} \times \mathbf{H} = 0 \quad \text{on} \quad \Gamma_{||},$$
$$\mathbf{n} \times \mathbf{A} = 0 \quad \text{on} \quad \Gamma_{\perp}. \tag{3}$$

Depending on whether the condition of electric insulation is applied to the boundaries parallel to the x- or y-direction, xy- or yx-polarisation data are obtained, respectively. At the top (Γ_{top}) and bottom boundaries (Γ_{bottom}) we impose boundary values in terms of the magnetic field induced in a horizontally layered half-space (Wait (1953)):

$$H_{\perp} = 1 \, Am^{-1} \quad \text{on} \quad \Gamma_{top},$$
$$H_{\perp} = H_j(z), \quad j = x, y \quad \text{on} \quad \Gamma_{bottom}. \tag{4}$$

For the construction of the full 3-D MT impedance tensor, both xy- and yx-polarization data are required. Arranging the x- and y-components of the electric and magnetic fields obtained for xy- and yx-polarization such that

$$\mathbf{E} = \begin{pmatrix} E_x(xy) & E_x(yx) \\ E_y(xy) & E_y(yx) \end{pmatrix} \tag{5}$$

$$\mathbf{H} = \begin{pmatrix} H_x(xy) & H_x(yx) \\ H_y(xy) & H_y(yx) \end{pmatrix}, \tag{6}$$

the impedance tensor $\mathbf{Z}$ can the be obtained by $\mathbf{Z} = \mathbf{E}\,\mathbf{H}^{-1}$. The off-diagonal elements of the impedance tensor are therefore

$$Z_{xy} = \frac{E_x(yx)H_x(xy) - E_x(xy)H_x(yx)}{H_x(xy)H_y(yx) - H_x(yx)H_y(xy)} \quad , \quad Z_{yx} = \frac{E_y(xy)H_y(yx) - E_y(yx)H_y(xy)}{H_x(xy)H_y(yx) - H_x(yx)H_y(xy)}. \tag{7}$$

For any period $T = 2\pi/\omega$, the apparent resistivity ρ_a and phase ϕ can then be calculated by

$$\rho_{xy} = \frac{1}{\omega\mu}|Z_{xy}|^2, \quad \rho_{yx} = \frac{1}{\omega\mu}|Z_{yx}|^2 \quad \text{and} \quad \phi_{xy} = arg(Z_{xy}), \quad \phi_{yx} = arg(Z_{yx}). \tag{8}$$

In the following, we use the terms *Zxy mode* or *Zyx mode* to distinguish xy- and yx-polarization from quantities derived by a combination of both (Nam et al. (2007)). An important property of time-harmonic EM field is the skin depth $\delta \approx 503\sqrt{\rho/f}$, where δ, the resistivity ρ and the frequency f are given in [m], [Ω m] and [Hz], respectively. is determined, whereas δ, the resistivity ρ and the frequency f are given in [m], [Ω m] and [Hz], respectively.

To solve the boundary value problem (1)-(4), the finite element method (FEM) is applied on unstructured tetrahedral meshes (see Börner (2010); Schwarzbach (2009)). Tetrahedral meshes are well suited for the spatial discretization of arbitrary 3-D geometries which occur when digital elevation models have to be incorporated into numerical simulations. In the 3-D simulations presented here, curl-conforming Nédélec elements with second-order basis functions are employed. In all experiments the FE discretization has been carried out using the Electromagnetics Module of the COMSOL Multiphysics package.

## 3 Description of the digital elevation model

The area used in the simulations extends from 38.4° to 39.2° N and 14.7° to 15.7° E. At 39° N, the distance between two degrees of latitude is 110.95 km, whereas the distance between two degrees of longitude is 86.51 km. Hence, the model area has a length of 86.51 km in the east-west (x) and 88.76 km in the north-south (y) direction.

We have used two sets of digital terrain data. The ETOPO1 data set is a 1 arc-minute model and provides elevation values for both land and sea. It is available online at the National Geophysical Data Center (http://www.ngdc.noaa.gov) and gives a good approximation for the regional bathymetry. Since,

however, its spatial data density is not sufficient to describe Stromboli's topography, a second data set has been used. These data are available from the Shuttle Radar Topography Mission (SRTM), a project to obtain high-resolution topographic data (http://srtm.csi.cgiar.org/). The horizontal resolution of the two data sets are listed in the following table. The digital elevation model for the area considered here has been obtained by blending both ETOPO1 and SRTM data sets.

	resolution x-direction	resolution y-direction
SRTM	0.0721 km	0.0925 km
ETOPO1	1.4419 km	1.8491 km

Interpolating the bathymetry data and fitting the two data sets along the coastlines leads to a digital elevation model as depicted in Fig. 2.
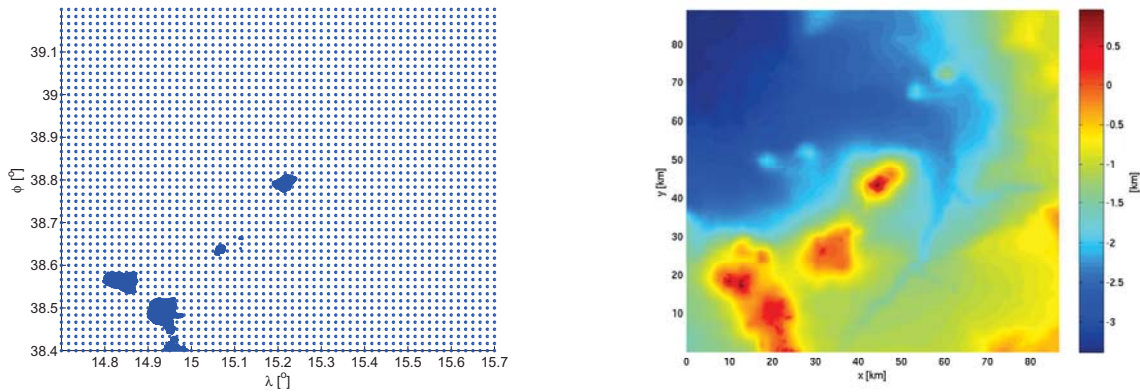
Figure 2: Data points obtained from ETOPO1 (coarse grid) and SRTM (fine grid resembling the islands) for bathymetry and topography (left), digital elevation model obtained by smooth interpolation onto the SRTM grid (right). Stromboli island is located at the centre of both images.

4 Numerical studies

The geometry of the volcanic island of Stromboli is incorporated into the simulation models in three different levels of increasing complexity. This approach enables us to better differentiate which part of the model has an influence on the electromagnetic fields and how distinct this influence is. The first model uses a frustum as the volcanic edifice embedded in a layered background consisting of an air layer, a sea layer and a substratum. In the second model the frustum is replaced with the topography of Stromboli. The edges of this topographic surface have been adjusted to the sea-floor. The third, most complex model uses both topography and bathymetry data.

For the numerical computations three different computer architectures have been used:

computer name	architecture	RAM
klio	4 Intel(R) Xeon(R) @ 3 GHz	16 GB
erato	4 Quad-Core AMD Opteron @ 2.5 GHz	128 GB
RM	56 nodes based on Intel Xeon (E5450 @ 3 GHz)	16 GB per 8-core blade

For each of the three models, apparent resistivities ρ_a and phases ϕ were calculated along profiles running along the sea-floor and over the slopes of the volcano for a period of $T = 10^3$ s. Furthermore, sounding curves were determined for selected sites on the sea-floor and on the volcano to demonstrate the dependency of ρ_a and ϕ on frequency.

4.1 Frustum model

The geometry and appropriate conductivities of the frustum model as well as a map of the locations of the sounding sites are depicted in Fig. 3. Since there are large conductivity contrasts between the

frustum, the sea and the air layer, a non-trivial behaviour of the electromagnetic fields is to be expected. The electric currents are mainly induced in the conductive sea layer and are compressed above the slopes. Moreover, the currents tend to concentrate below the sea surface due to the skin effect.

Due to horizontal conductivity contrasts, electric charges accumulate at the interfaces between the volcano and the sea layer. Their surface density is proportional to $-\mathbf{E} \cdot \nabla\sigma$. Therefore, an additional electric field is generated which leads to an increase of the total electric field towards the top of the volcano (around $x = \pm 0.5\,\mathrm{km}$ in the profile, Fig. 4) and to a decrease towards the sea-floor (around $x = \pm 5.6\,\mathrm{km}$ in the profile). This static shift effect results in discontinuities of the apparent resistivity at the base points of the frustum on the sea-floor, at the coastline points and at the top of the volcano. Unlike the apparent resistivity, the phase has a more continuous behaviour and appears to be a rather robust parameter even for pronounced topography. 40 km away from the center of the volcano $(x, y = \pm 40\,\mathrm{km})$, both phase and apparent resistivity reach their values expected for the half-space $(45°, 100\,\Omega\,\mathrm{m})$.
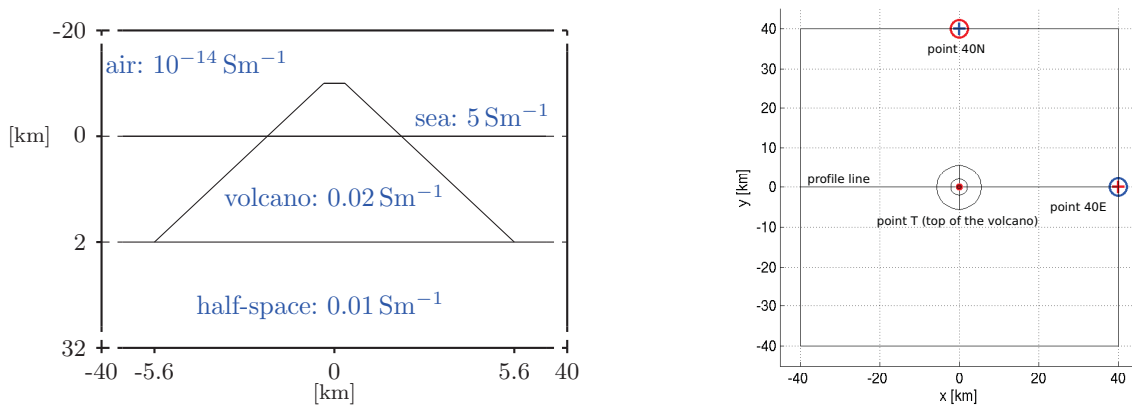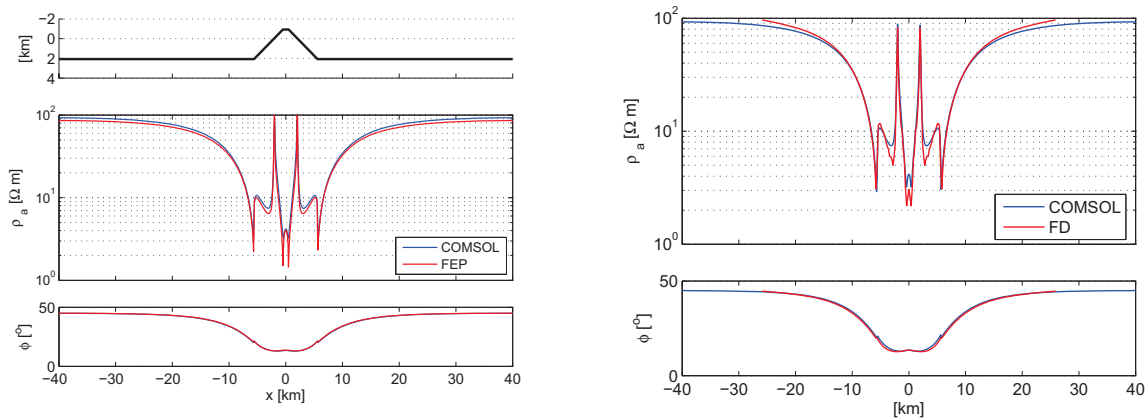

Figure 3: Vertical cross-section through the frustum model (left) and plan view of the model domain (right) showing the locations of the sounding curves (T, N40, E40).

To verify our results, two independent numerical codes have been used to provide reference datasets for the frustum model. More precisely, data have been obtained using a finite element package (FEP) by Schwarzbach (2009), and a finite difference package (FD) by Mackie et al. (1994).

A comparison of the apparent resistivities with those obtained by FEP reveals that they slightly differ near the boundaries of the model and at the lower part of the volcano slopes (Fig. 4, left), where ρ_a is lower for FEP. Moreover, the peaks at the base of the frustum, at the coastline points and at the edges of the plateau are even more pronounced for FEP. Here, we assume an influence of the different spatial discretization of the model. The curves of the phase are nearly congruent for both FE codes.

Apparent resistivities and phases obtained by FD (Fig. 4, right) show similar features in general. However, there are significant differences along the slopes of the volcano. We attribute this to the fact that in the FD code considered here electric field components are located perpendicular to cell faces of a rectangular cartesian grid. Problems in interpolating the discrete electric field components at the desired positions along the volcano slopes are thus to be expected. Finite element techniques on unstructured grids clearly show their superiority in this respect.

23. Schmucker-Weidelt-Kolloquium für Elektromagnetische Tiefenforschung,
Heimvolkshochschule am Seddiner See, 28 September - 2 Oktober 2009

63

Figure 4: Comparison of the profile curves of the frustum model, $T = 10^3$ s.

Fig. 5 depicts three sounding curves for the sites on top (point T in Fig. 3) and 40 km away from the volcano (E40, N40 in Fig. 3).

Sounding curves for the volcano site T are displayed for periods between 10^{-3} and 10^3 s (Fig. 5, left). For short periods, where the skin depth is small ($\delta \approx 355$ m for $50\,\Omega$ m and 10^{-2} s), the resistivity of the volcano is reproduced and the phase reaches values around 45°. For periods between 10^{-1} s and 10^2 s, the influence of the conductive sea layer is dominant and therefore, the apparent resistivity decreases whereas the phase increases. For longer periods the resistive half-space dominates the curves ($\delta \approx 16$ km for $100\,\Omega$ m and 10^3 s). The sounding curves for the two sites on the sea-floor are displayed for a subset of the full period range (between 10^1 and 10^3 s) because of the strong attenuation within the very conductive sea water (Fig. 5). High frequencies generally require a much finer spatial discretization in regions where the skin depth is small. However, the computational experiments have been carried out on a mesh well suited for mid to low frequencies. Results for high frequencies were not satisfactory for the coarse meshes used here, and thus have not been included in the comparison.

The long period ends of the sounding curves nicely approach the values of the lower half-space, i.e. $100\,\Omega$m for ρ_a and about 45° for ϕ. For short periods there are deviations from these values, which are larger for the points on the profiles oriented perpendicular to the component of the driving electric field, i.e. for point E40 at $y = 40$ km for ρ_{xy} and the point at $x = 40$ km for ρ_{yx} (cross markers in Fig. 5, cf. Fig. 3, right). As mentioned above, these deviations are due to the insufficient spatial discretization for short periods in regions of strong attenuation.
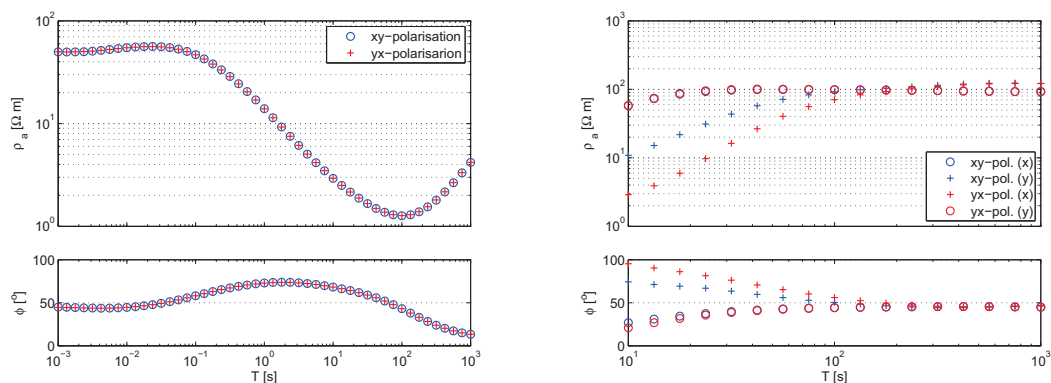
Figure 5: Sounding curves for the volcano site T (left) and the sea-floor sites E40 and N40 (right) for the frustum model. Here, xy-pol. and yx-pol. refer to ρ_{xy} and ρ_{yx}, resp.

The following table summarizes important computational parameters for the three different codes, such as polynomial degree of the basis functions (BFD) for the FE method and degrees of freedom (DOF). The overall CPU time required to obtain the result for one frequency was in the order of two minutes. The total time required to compute all field components for one polarization sums up to

23. Schmucker-Weidelt-Kolloquium für Elektromagnetische Tiefenforschung,
Heimvolkshochschule am Seddiner See, 28 September - 2 Oktober 2009

64

about two hours for all 49 frequencies for the FE codes and 30 minutes for the FD code. Note that the 3-D impedance requires the calculation of both polarizations (see eq. (7)).

|	computer	CPUs	BFD	elements	DOFs	time [min]
COMSOL Multiphysics®						
xy-pol.	*klio*	4	quadratic	82 661	523 580	119,56
FEP						
xy-pol.	*erato*	8	quadratic	57 666	434 456	119,07
FD code						
	FD code	131 x 131 x 154 grid cells + 15 air layers				≈ 30

4.2 Stromboli-Topography model

In the second level of complexity, a realistic topography of Stromboli is incorporated. Since this topography is smoothly adjusted to the flat sea-floor, the edifice is larger in this model than in reality. Furthermore, the conductivity of the volcano has been reduced to $0.01\,\mathrm{Sm^{-1}}$.

Figs 6 and 7 illustrate the model with the positions of the profiles and the locations for which sounding curves have been calculated. Sounding curves are shown for sites a, N and E only.
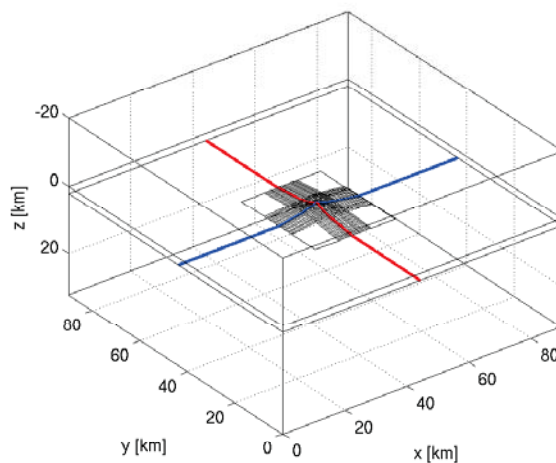
Figure 6: Flat sea-floor model including the real topography of Stromboli island. Red and blue lines indicate the x- and y-profiles, respectively.
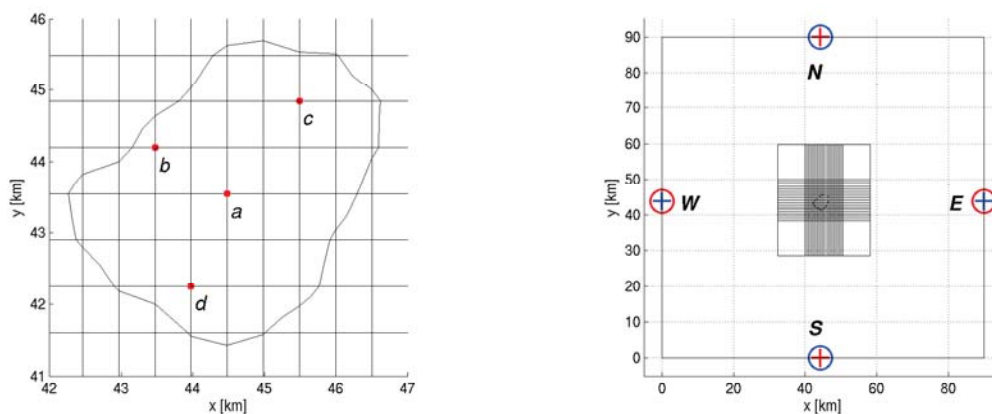
Figure 7: Locations for which sounding curves are computed are denoted by a, b, c, d on the island (left) and N,E,S,W on the sea-floor (right).

Fig. 8 displays the apparent resistivities ρ_{xy} and phase Φ_{xy} for $T = 10^3\,\mathrm{s}$ along two profiles aligned with the x-axis (x-profile) and the y-axis (y-profile). The apparent resitivity for the x-profile is associated

23. Schmucker-Weidelt-Kolloquium für Elektromagnetische Tiefenforschung,
Heimvolkshochschule am Seddiner See, 28 September - 2 Oktober 2009

65

with the xy-impedance tensor elements (Zxy mode) while the apparent resistivity for the y-profile is derived from the yx-elements (Zyx mode). The curves for both Zxy and Zyx modes show similar features. This can be explained by the similar topography along the two different profiles. Nevertheless, the extent of the volcano's edifice in y-direction is larger than in x-direction. Hence, the corresponding minima and maxima of the curves are shifted relative to each other.

Due to the smoother transition of the topography from the sea-floor to the volcano slopes the peaks at the base points of the edifice are not as pronounced as for the frustum model. Since there is no volcano plateau in the x-profile, there is just one minimum at $x \approx 44 \, \text{km}$ for ρ_{xy}.

As for the frustum model, the sounding curves for the volcano (e.g. for site a in Fig. 9, left) reflect the layering of the earth with regard to the electrical conductivity whereas long periods correspond to large skin depths. Since the same conductivity is assigned to the volcano and the half-space the sounding curves reach values around $100 \, \Omega \, \text{m}$ for short periods.

Due to the asymmetry of the model, offsets occur between the curves derived from Z_{xy} and Z_{yx} that are higher for ρ_a than for ϕ. Hence, it can be assumed that the phase is less affected by these two aspects.

The sounding curves for the sea-floor are displayed in Fig. 9 (right). Since the edifice is larger than the one represented by the frustum the long period apparent resitvities deviate more significantly from the undisturbed half-space values.
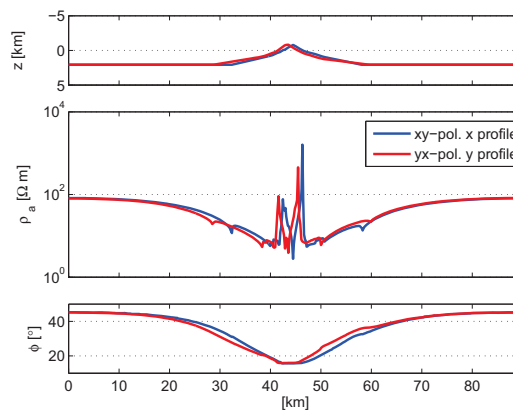
Figure 8: Topography (top), apparent resistivity (center), phase (bottom), derived from Z_{xy} and Z_{yx} (xy- and yx-pol., resp.) along the x- and the y-profile for $T = 10^3 \, \text{s}$.

The differences in the short period range may again be attributed to the insufficient spatial discretization.
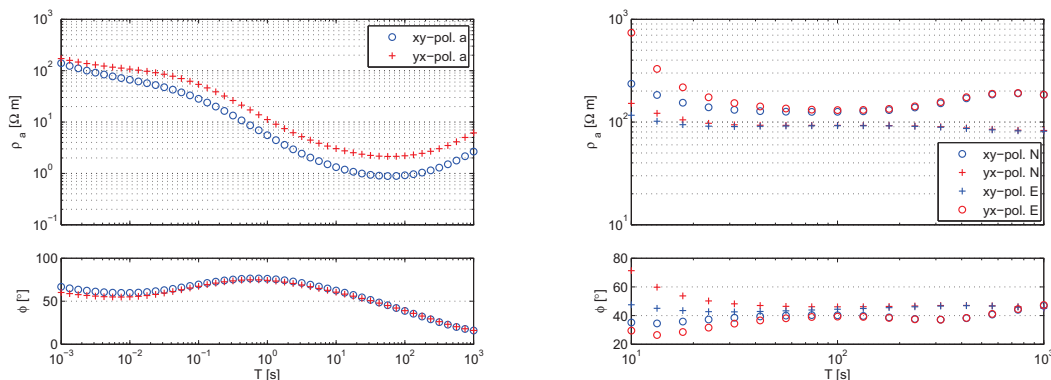
Figure 9: Sounding curves for the island site a (left) and for the sea-floor sites N and E (right). xy-pol. and yx-pol. refer to Z_{xy} and Z_{yx}, resp.

The incorporation of the detailed Strombolian topography leads to a massively increasing number of mesh points. In order to keep computational costs low the meshes for computing the full sounding

23. Schmucker-Weidelt-Kolloquium für Elektromagnetische Tiefenforschung,
Heimvolkshochschule am Seddiner See, 28 September - 2 Oktober 2009

66

curves were coarsened.

|	Computer	CPUs	BFD	No. of elements	DOFs	Time [min]
			profile curves			
xy-pol.	*erato*	8	quadratic	443 563	2 823 488	114.78
			sounding curves			
xy-pol.	*erato*	8	quadratic	164 662	1 048 116	≈ 721

4.3 Bathymetry-Topography model

In the third level of complexity, the topography of the island is incorporated as well as the regional bathymetry including the other Liparian islands. This allows to analyse the effect on the electromagnetic fields not only due to the volcano itself but also due to the variable thickness of the sea layer.

Figs 10 and 11 illustrate the model and the locations of the profiles and points for which sounding curves have been calculated. As an example, apparent resistivities and phases for a period of 1000 s are shown for the xN- and xS-profiles as well as the full sounding curves for points a, c, N and S.
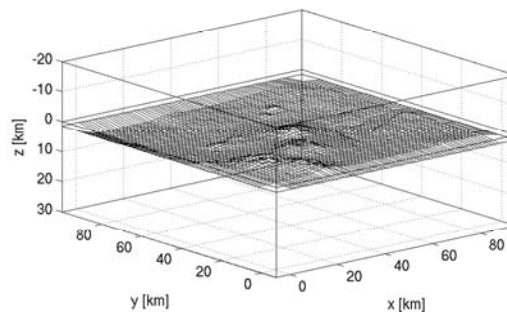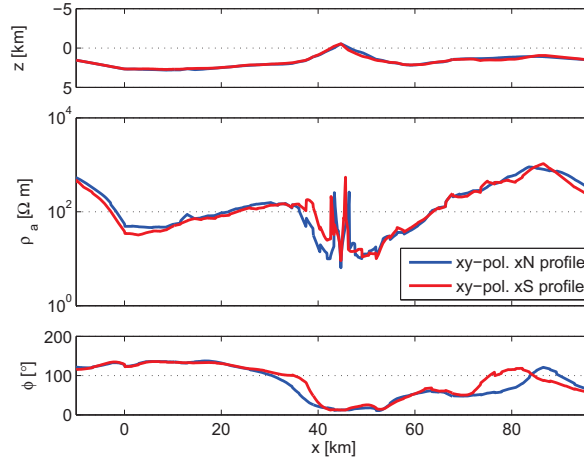

Figure 10: Model including the regional bathymetry and the topography of Stromboli and the Liparian Islands.
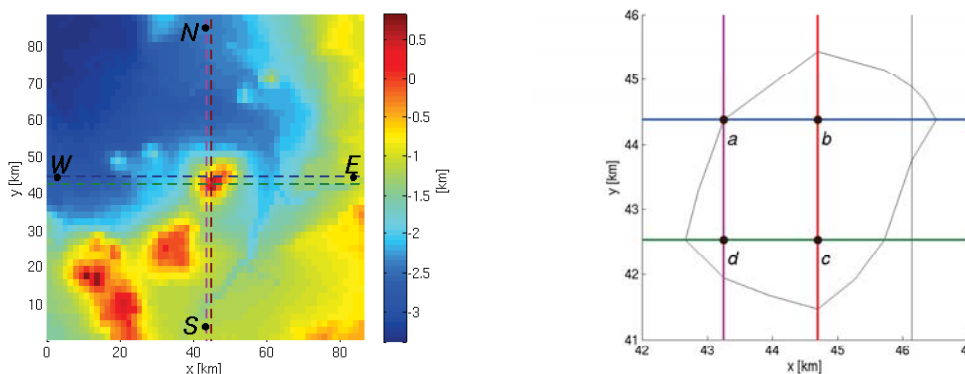

Figure 11: Left: Elevation map inferred from digital terrain data showing the locations of seafloor sounding points N, E, S, W and the profile lines xN, xS in the EW-direction and yE, yW in the NS-direction. Right: Coast line of Stromboli and locations of sounding points a, b, c, d.

The xN and xS profiles running East-West in parallel (Fig. 12) are close to each other. Hence, the features of the respective apparent resistivity and phase curves are similar. As for the previous models, peaks at the coastline and at the top of the volcano can be observed. However, serious perturbations are provoked by the regional bathymetry. Induced currents are vertically compressed in the shallow parts of the ocean yielding higher apparent resistivities. Vice versa, apparent resistivites are decreased in deep water areas. The soundings at site c (Fig. 13, right) again show the influence of the volcano,

23. Schmucker-Weidelt-Kolloquium für Elektromagnetische Tiefenforschung,
Heimvolkshochschule am Seddiner See, 28 September - 2 Oktober 2009

67

Figure 12: Topography (top), apparent resistivity (center) and phase (bottom) for $T = 10^3$ s at profiles xS and xS. xy-pol. and yx-pol. refer to Z_{xy} and Z_{yx}, resp.
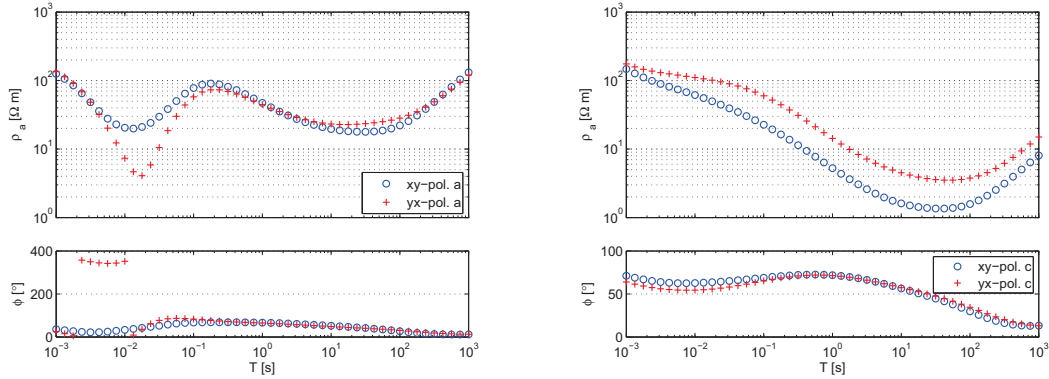
Figure 13: Sounding curves for the island sites a (left) and c (right). xy-pol. and yx-pol. refer to Z_{xy} and Z_{yx}, resp.

the sea layer and the half-space for the appropriate period ranges. However, at site a, which is located directly at the coastline, the sea layer affects the curves already for shorter periods, especially for the Zyx mode. Still, for periods longer than $T = 10^{-1}$ s the shapes of the curves are similar to those at point c (although shifted to higher ρ_a-values).
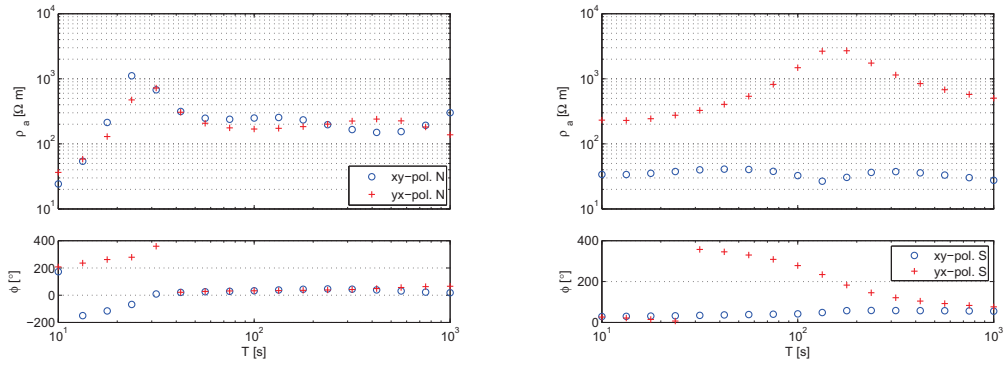
All curves derived from Z_{xy} and Z_{yx} show an offset which can be attributed to the asymmetric elevation data used in the MT simulations.

For the two sea-floor sites N and S the topography effect varies for the two cases considered (Fig. 14). Site N (Fig. 14, left) is located at greatest distance from the islands. Therefore, the curves are similar to those obtained using the simpler models and for longer periods they are almost assume the corresponding half-space values.

The sounding curves at site S (Fig. 14, right) seem to be affected by two different facts. For ρ_{xy} the graben-like structure in this area (cf. Fig. 11, left) leads to lower apparent resistivities. On the other hand, the more resistive islands affect the ρ_{yx}-curves.

We note that the out-of-quadrant phases in Fig. 14 occur mainly at the high frequencies, which indicates that the mesh used for the numerical computations is still not fine enough to obtain results with the desired accuracy.

The following table summarizes the mesh properties and CPU times associated with the bathymetry-topography model.

23. Schmucker-Weidelt-Kolloquium für Elektromagnetische Tiefenforschung,
Heimvolkshochschule am Seddiner See, 28 September - 2 Oktober 2009

68

Figure 14: Sounding curves for the sea-floor sites N (left) and S (right). xy-pol. and yx-pol. refer to Z_{xy} and Z_{yx}, resp.

	Computer	CPUs	BFD	No. of elements	DOFs	Time [min]
			profile curves			
xy-pol.	*erato*	16	quadratic	546 759	3 479 830	44.41
			sounding curves			
xy-pol.	*erato*	16	quadratic	312 721	1 987 514	≈ 1103

5 Conclusions

In this work, distortion effects on MT data caused by topography and bathymetry are examined for the area around Stromboli. The geometry of Stromboli has been incorporated into FE simulations applying three different levels of increasing complexity.

In the first model, a frustum representing the volcano has been embedded in a layered background. This model yields a non-trivial apparent resistivity profile curve which is mainly dominated by peaks at the base points of the frustum, at the coastline points and at the edges of the volcano plateau. These are caused by static shift effects and the high conductivity contrast between the volcano and the sea layer. The results of the frustum model have been verified by a finite element code by Schwarzbach (2009) and a finite difference code by Mackie et al. (1994).

For the second model of Stromboli digital elevation data of the island have been included in the model geometry. Compared to the frustum model, the apparent resistivity and phase curves along the profiles and the sounding curves for the volcano show similar features.

Finally, digital bathymetry data have been added to the third, most complex Stromboli model to take into account realistic topography and bathymetry features of the region. The apparent resistivity still shows the characteristic peaks at the coastline points for most of the profiles. The effects of the bathymetry and topography of the surrounding islands are superposed, which results in very complicated profile and sounding curves.

These results clearly point out that topography and bathymetry can heavily distort MT data and thus need to be considered for an accurate numerical interpretation of MT measurements.

Finally, we emphasize that FE methods on unstructured grids provide a sophisticated tool for treating problems associated with complex geometry.

Acknowledgements

23. Schmucker-Weidelt-Kolloquium für Elektromagnetische Tiefenforschung,
Heimvolkshochschule am Seddiner See, 28 September - 2 Oktober 2009

69

References

Börner, R.-U. (2010). *Numerical Modelling in Geo-Electromagnetics: Advances and Challenges*. Surveys in Geophysics 31(2): 225–245.

Mackie, R. L., J. T. Smith, and T. R. Madden (1994). *Three-dimensional electromagnetic modeling using finite difference equations: The magnetotelluric example*. Radio Science 29(4): 923–935.

Nam, M. J., H. J. Kim, Y. Song, T. J. Lee, J.-S. Son, and J. H. Suh (2007). *3D magnetotelluric modelling including surface topography*. Geophysical Prospecting (55): 277–287.

Schwarzbach, C. (2009). *Stability of Finite Element Solutions to Maxwell's Equations in Frequency Domain*. PhD thesis. TU Bergakademie Freiberg.

SwissEduc (2010). *SwissEduc: Stromboli Online - Die Insel*. URL: http://www.swisseduc.ch/stromboli/volcano/geogr/aerial-de.html.

Wait, J. R. (1953). *Propagation of radio waves over a stratified ground*. Geophysics 18(2): 416–422.

Wikipedia (2010). *Liparische Inseln*. URL: http://de.wikipedia.org/wiki/Liparische_Inseln.